Separation and Purification Technology 394 (2026) 137342

Contents lists available at ScienceDirect

Separation and Purification Technology

journal homepage: www.elsevier.com/locate/seppur

Ternary $CuNi_3Co$ alloy electrodes boost selective electrocatalytic reduction of nitrate in complex scenarios

Jifa Zhang [a], Yihang Wang [a], Jiantao Xu [a], Pengcheng Yin [a], Yongjie Chen [a], Jianghua Yu [a], Dawei Li [a,*], Feihu Li [a,b]

[a] Collaborative Innovation Center of Atmospheric Environment and Equipment Technology, Jiangsu Key Laboratory of Atmospheric Environment Monitoring and Pollution Control, School of Environmental Science and Engineering, Nanjing University of Information Science and Technology, 219 Ningliu Road, Nanjing 210044, China

[b] NUIST Reading Academy, Nanjing University of Information Science and Technology, 219 Ningliu Road, Nanjing 210044, China

ARTICLE INFO

Editor Name: Jorge Bedia

Keywords:
Electrochemical denitrification
Nitrate reduction
Cu–Ni–Co ternary alloy
Nickel foam
Chloride-containing wastewater

ABSTRACT

A fast, efficient, and durable cathode is essential for electrocatalytic nitrate reduction (NO_3RR) and nitrate removal in complex wastewaters. Herein, a self-supported $CuNi_3Co$@NF cathode was fabricated by directly co-depositing Cu–Ni–Co ternary metallic microparticles onto three-dimensional (3D) nickel foam (NF). Morphological characterization confirms the uniform dispersion of Cu–Ni–Co microparticles across the NF skeleton. Compared with monometallic and bimetallic counterparts, $CuNi_3Co$@NF exhibits markedly enhanced intrinsic NO_3RR performance in Cl^--free electrolyte, achieving near-complete NO_3^-–N removal (99.99%) with high NH_4^+ selectivity (98%) as the dominant dissolved product. In chloride-containing wastewater, the system can be operated as a coupled electrochemical–chemical (EC–C) denitrification process, where the cathode efficiently reduces NO_3^- to reduced nitrogen species while anodically generated active chlorine species promotes further conversion toward gaseous nitrogen products, resulting in high NO_3^-–N removal (up to 98%) and high TN removal. In addition, $CuNi_3Co$@NF maintains stable performance over a broad range of initial nitrate concentrations (50–300 mg L^{-1} NO_3^-–N) and solution pH values (3–12), and retains its activity over ten consecutive cycles, demonstrating strong durability under saline and pH-challenging conditions.

1. Introduction

Nitrate (NO_3^-), a typical nitrogenous pollutant originating from agricultural fertilization, livestock wastewater, and effluents from chemical and metallurgical industries, has become one of the most prevalent inorganic nitrogen species in aquatic environments around the world [1]. Excessive discharge of NO_3^- into surface and groundwater causes eutrophication and ecological imbalance, and may enter the human body through drinking water, posing severe health risks such as methemoglobinemia and increased susceptibility to gastrointestinal cancers [2]. Therefore, efficient, economical, and selective removal of NO_3^- in complex water matrices under complex conditions is crucial for environmental protection and public health.

Current technologies for nitrate remediation include biological denitrification, ion exchange, membrane separation, and chemical reduction [2–4]. Although biological processes are effective at low NO_3^- concentrations, they are highly sensitive to temperature, carbon supply, and dissolved oxygen, suffering from long start-up periods and often failing to operate under high salinity, toxic contaminants, or shock loads [5]. Ion-exchange and membrane-based technologies offer high separation efficiency but essentially "transfer" rather than "eliminate" nitrate, causing secondary pollution during resin regeneration or concentrate discharge, alongside high energy and operating costs [6]. Chemical reductants and advanced oxidation processes typically require substantial chemical input or complex catalysts, making it difficult to precisely control reaction pathways and terminal products under continuous-flow conditions [7]. These limitations underscore the need for more controllable and environmentally friendly strategies.

Electrochemical nitrate reduction (NO_3RR) has emerged as a promising alternative owing to its simple equipment, operation under ambient conditions, use of electrons as clean reagents, and its precise controllability of reaction pathways via potential or current manipulations [8–10]. In a typical NO_3RR process, the cathode drives multi-

* Corresponding author.
E-mail address: daweili@nuist.edu.cn (D. Li).

https://doi.org/10.1016/j.seppur.2026.137342
Received 30 December 2025; Received in revised form 13 February 2026; Accepted 19 February 2026
Available online 21 February 2026

electron (e^-)/proton (H^+) transfer steps, converting NO_3^- into various products such as N_2, NH_4^+, and N_2O. Among them, N_2 is the most desirable end product, while NH_4^+ can be recovered as a value-added nitrogen resource [11]. However, the NO_3RR involves a complex reaction network with multiple intermediates (e.g., NO_2^-, NO, NH_2OH) and competes strongly with the hydrogen evolution reaction (HER), which makes the design of electrocatalysts with high activity, selectivity, and Faradaic efficiency highly challenging so far [12]. The configuration, composition, and surface electronic structure of the cathode are the key parameters of the NO_3RR pathway and product distribution. Rational optimization of these parameters is a promising strategy for highly selective and efficient NO_3RR in complex wastewater scenarios.

Of various electrode materials, transition metals and their alloys—with tunable valence states and abundant catalytic activity—have attracted considerable attention [13,14]. For instance, copper (Cu) exhibits strong adsorption and activation of NO_3^-, often yielding high conversion rates, but is prone to NO_2^- or NH_4^+ accumulation [15]. Nickel (Ni) provides excellent electrical conductivity and structural stability, supplying continuous electron pathways and *H species, but suffers from insufficient NO_3^- adsorption/activation capability [16]. Cobalt (Co), on the other hand, shows superior activity in hydrogenation and multi-electron processes, enhancing the deep reduction of intermediates [17]. Recent studies attempted to introduce synergistic effects through creating binary alloys such as CuNi or NiCo alloys, offering facile tailorability of reaction pathways and, therefore, the composition of end products [18–20]. Nevertheless, these binary alloy systems often suffered from undesired NO_2^- accumulation, low selectivity, and insufficient stability in high-salinity environments.

In this regard, ternary alloys offer greater freedom for "electronic structure engineering" and "division-of-function synergy" than mono- or binary systems. Rationally incorporating a third component can regulate *d*-band filling and metal–N/O bond strengths, thereby optimizing NO_3^- adsorption and intermediate stability [21]. Meanwhile, different metals may separately contribute to NO_3^- activation, *H supply, hydrogenation, and HER suppression, providing the structural basis for efficient and controllable NO_3RR [22,23]. To date, few studies have directly constructed binder-free ternary alloys on three-dimensional conductive scaffolds (e.g., nickel foam, NF) with tunable composition for NO_3RR. Yet, the mechanisms for highly selective NO_3RR on such ternary alloy electrodes remain less explored, particularly in complex water matrices with high salinity (1500 ppm of Cl^-).

Herein, we aim to explore the rational construction of ternary alloy electrodes for highly selective and efficient NO_3RR in complex wastewater environments (i.e., high salinity). Specifically, we developed a binder-free Cu–Ni–Co ternary alloy electrode (denoted as $CuNi_3Co$@NF) by co-electrodepositing Cu–Ni–Co microparticles onto a three-dimensional NF scaffold in a citrate-sulfate mixture. By optimizing the metal-ion ratios and electrodeposition parameters, electrodes with a highly roughened heterostructure were obtained. Subsequently, the ternary alloy electrodes were comprehensively evaluated by comparing their NO_3RR performance with the NF, and a binary electrode (denoted as CuNi@NF) under Cl^--free conditions. The effects of initial NO_3^-–N concentration, Cl^- concentration, and pH on NO_3^- removal and total nitrogen reduction were systematically evaluated in high-saline wastewaters. Based on a spectrum of spectroscopic data, the synergistic mechanisms for NO_3RR were identified. This work provides new insights into the rational structural optimization of ternary alloy electrodes and their applications in high-saline nitrate-containing wastewater remediation.

2. Experimental section

2.1. Chemicals

Commercial nickel foam (NF, thickness: 2 mm, porosity ≥98%; Kunshan Tanqianlang Co., China) and graphite plate electrodes (Tianwang Graphite Products, Dongguan, China) were used as alloy scaffolds and anode, respectively. All chemicals including copper sulfate pentahydrate ($CuSO_4·5H_2O$, ≥99.0%), nickel sulfate hexahydrate ($NiSO_4·6H_2O$, ≥98.5%), cobalt nitrate hexahydrate ($Co(NO_3)_2·6H_2O$, ≥98.5%), trisodium citrate, boric acid, sodium dodecyl sulfate (SDS), sodium sulfate (Na_2SO_4, ≥99.0%), thiourea, acetone, and anhydrous ethanol were obtained from Sinopharm Chemical Reagent Co., Ltd. (Shanghai, China), and used without further purification. All solutions were prepared using ultrapure deionized water (DI H_2O, 18.2 MΩ·cm, 25 °C).

2.2. Preparation of $CuNi_3Co$@NF electrodes

The $CuNi_3Co$@NF cathode was synthesized via a galvanostatic co-deposition method [24]. Briefly, a piece of NF substrate (3 × 2.5 cm^2) was first ultrasonically cleaned in acetone for 15 min to remove residual organic contaminants, rinsed thoroughly with DI water and ethanol, and then polished in 1.0 M H_2SO_4 for 120 s to eliminate surface oxide layers. After acid polishing, the NF scaffolds were rinsed repeatedly with DI water until neutral.

The electrodeposition was performed in a bath containing 0.2 M Ni^{2+}, 0.04 M Co^{2+}, 0.01 M Cu^{2+}, 0.36 M trisodium citrate, 0.4 M H_3BO_3, and 10 mg SDS, with the pH adjusted to 5.0. Specifically, the polished nickel foam (NF) was used as the cathode, and two graphite plates on both sides served as the anodes for the dual-anode electrodeposition experiment (Fig. 1a). Electrochemical co-deposition was carried out in a 45 °C water bath under a constant current density of 25 mA cm^{-2} for 45 min. After deposition, the samples were rinsed with DI water, dried with nitrogen, and stored in a vacuum oven for subsequent use. For comparison, a binary alloy (denoted as CuNi@NF) was also prepared following the same method. The optimization of the preparation of the ternary metal alloy electrodes is detailed in Text S1–5 (Supporting Information).

2.3. Material characterization

X-ray diffraction (XRD) was performed on an XRD-6100 (Shimadzu, Japan) diffractor with Cu Kα radiation, and at a tube voltage of 40 kV and a tube current of 30 mA. Surface morphology was examined using a Gemini 300 field emission scanning electron microscope (SEM, ZEISS, Germany) equipped with an energy dispersive X-ray detector (EDX). X-ray photoelectron spectroscopy (XPS) data were collected on a UIVAC-PHI system equipped with a 300 W Al Kα source, and all spectra were calibrated using the C 1 s peak at 284.8 eV.

Electrochemical measurements were carried out using a CS310H workstation (CorrTest Instruments, China) with a three-electrode configuration in a 50 mM Na_2SO_4 solution at room temperature (RT). The as-prepared electrodes (10 × 10 mm^2) served as the working electrodes, while an Ir–Ru/Ti plate (10 × 20 mm^2) and a saturated calomel electrode (SCE) were used as the counter and reference electrodes, respectively. Double-layer capacitance (C_{dl}) was determined from cyclic voltammetry (CV) curves collected in the non-Faradaic region (−0.3 to 0 V) at scan rates of 10, 20, 40, 60, 80, and 100 mV s^{-1}, respectively [25]. To evaluate the electrochemical NO_3RR behavior, CV scanning from −1.5 to 0 V at 50 mV s^{-1} was conducted in the presence or absence of 100 mg L^{-1} NO_3^-–N. Electrochemical impedance spectroscopy (EIS) was recorded from 10^5 to 0.01 Hz using a 5 mV AC perturbation at open-circuit potential [26].

2.4. Electrocatalytic nitrate reduction(NO_3RR) experiments

Electrocatalytic NO_3RR experiments were performed in a 150 mL homemade cell under magnetic stirring at 200 rpm. A total of 100 mL electrolyte containing a given concentration of NO_3^-–N and 50 mM Na_2SO_4 was employed, and NaCl was added when chloride-containing

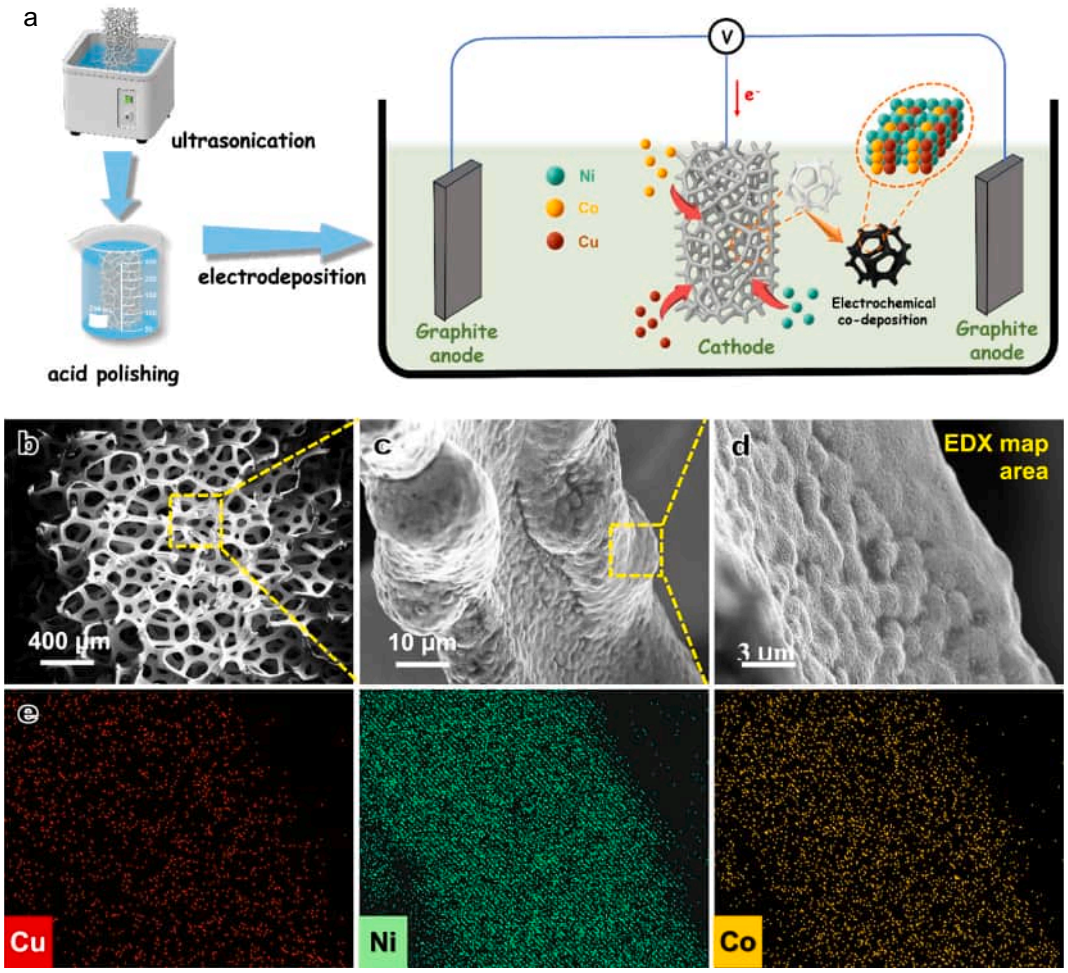

Fig. 1. (**a**) Schematic illustration of the preparation of $CuNi_3Co$@NF electrode; (**b–d**) SEM images of the as-prepared $CuNi_3Co$@NF; (**e**) EDX elemental mapping showing the uniform distribution of Cu, Ni, and Co atoms on the surface of the NF scaffolds.

conditions were required. The $CuNi_3Co$@NF electrode was used as the cathode and an Ir–Ru/Ti plate as the anode, with an inter-electrode spacing of 2 cm. The electrolysis was conducted in an undivided (membrane-free) configuration under continuous stirring (200 rpm), which minimizes macroscopic concentration polarization and ensures a continuous supply of NO_3^- to the cathode by convection and diffusion. The short inter-electrode distance (2 cm) was also selected to reduce ohmic loss in the membrane-free cell. In Cl^--free electrolyte, the anodic reaction is dominated by OER, whereas in a chloride-containing electrolyte, chloride oxidation (competing with OER) can generate active chlorine species (Cl_2/HOCl/OCl^-). A DC power supply (ATTEN PPS3005T-3S, China) provided a constant current for electroreduction. The solution pH was adjusted using 0.2 M NaOH or 0.2 M H_2SO_4.

The concentrations of nitrate nitrogen (NO_3^--N), ammonium nitrogen (NH_4^+-N), nitrite nitrogen (NO_2^--N), and total nitrogen (TN) were quantified using a UV–Vis spectrophotometer. Specifically, NO_3^--N was determined using dual-wavelength UV detection at 220 and 275 nm (detection limit: 0.08 mg-N L^{-1}), NH_4^+-N was measured by the Nessler's reagent method at 420 nm (detection limit: 0.025 mg-N L^{-1}), while NO_2^--N was measured using the N-(1-naphthyl)ethylenediamine method at 540 nm (detection limit: 0.003 mg-N L^{-1}), and TN was determined via alkaline potassium persulfate digestion followed by UV detection at 220 and 275 nm (detection limit: 0.05 mg-N L^{-1}). All measurements were repeated thrice, and average values are reported.

The nitrate removal efficiency, total nitrogen removal efficiency, product selectivity, nitrogen gas generation, and Faradaic efficiency (FE) for NH_4^+ production were calculated separately using the following Eqs. (1–6):

$$R\left(NO_3^- - N\right) = \frac{C\left(NO_3^- - N\right)_0 - C\left(NO_3^- - N\right)_t}{C\left(NO_3^- - N\right)_0} \times 100\% \quad (1)$$

$$G\left(NO_2^- - N\right) = \frac{C\left(NO_2^- - N\right)_t}{C\left(NO_3^- - N\right)_0} \times 100\% \quad (2)$$

$$G\left(NH_4^+ - N\right) = \frac{C\left(NH_4^+ - N\right)_t}{C\left(NO_3^- - N\right)_0} \times 100\% \quad (3)$$

$$G(N_2) = R\left(NO_3^- - N\right) - G\left(NO_2^- - N\right) - G\left(NH_4^+ - N\right) \quad (4)$$

$$R(TN) = \frac{C\left(NO_3^- - N\right)_0 - C(TN)_t}{C\left(NO_3^- - N\right)_0} \times 100\% \quad (5)$$

$$FE_{NH_4^+ - N}(\%) = \frac{8FC_{NH_4^+ - N}V}{14 \times 1000 \times It} \times 100\% \quad (6)$$

where $(NO_3^-\text{-N})_0$ is the initial concentration of nitrate nitrogen, $(NO_3^-\text{-N})_t$, $(NO_2^-\text{-N})_t$, $(TN)_t$, and $(NH_4^+\text{-N})_t$ are the concentration (mg L^{-1}) of nitrate, nitrite, and ammonia at time ***t,*** respectively. $C_{NH_4^+ - N}$ is the ammonium concentration (mg L^{-1}), and ***V*** is the volume of electrolyte (L). It should be noted that Eq. (4) is only used for estimating gaseous nitrogen formation by nitrogen balance in the Cl^--free system. Under

Cl^--containing conditions, TN removal is used as the primary performance metric, and no specific gaseous product is assigned.

3. Results and discussion

3.1. Alloy composition and electrodeposition parameter optimization

To achieve optimal NO_3RR activity and durability, the effects of metal ion ratio in the parent electrolytes and the corresponding electrodeposition parameters (i.e., mode, current density, time, and temperature) were systematically investigated and optimized (Text S1–5, Fig. S1–S5, Supporting Information). Regarding metal ion composition, increasing Ni^{2+} concentration from 0.12 M to 0.20 M significantly improved NO_3^-–N removal rate and apparent rate constant, with further increase to 0.25 M yielding negligible improvement (Fig. S1a–b). Likewise, attempts to optimize Cu^{2+} and Co^{2+} ratios showed a typical "volcano-type" relationship. Specifically, insufficient introduction of Cu^{2+} and/or Co^{2+} ions into the parent electrolytes reduces synergistic efficiency, while excessive addition of both ions adversely impacts the NO_3RR performance with enhanced competitive hydrogen evolution reaction (HER) [27]. Considering NO_3^-–N removal efficiency, the pseudo-first-order rate constants (Fig. S1), and the Faradaic efficiency (FE%, Figs. S2–5), the optimal parent metal ions composition was determined as 0.01 M Cu^{2+}: 0.20 M Ni^{2+}: 0.04 M Co^{2+} in the electrodeposition bath.

Electrodeposition parameters were optimized subsequently based on the above optimal metal ion ratio in the parent electrolyte. For instance, dual-anode galvanostatic deposition produced more uniform and defect-free coatings than single-anode setups, yielding higher NO_3RR performance and NH_4^+ Faradaic efficiency under identical conditions (Fig. S2) [28]. Following the same criteria as specified above, current density, deposition time, and temperature were optimized to be 25 mA cm^{-2}, 45 min, and 45 °C, respectively, leveraging the coating coverage, roughness, and avoiding thick layers, dendrite growth, or composition segregation (Fig. S3–5) [29–31]. Given the best NO_3RR performance, the ternary alloy electrodes were then prepared under these optimized conditions: 0.01 M Cu^{2+}: 0.20 M Ni^{2+}: 0.04 M Co^{2+}, dual-anode, 25 mA cm^{-2}, 45 °C, and 45 min (Text S1-S5), yielding the optimal ternary alloy denoted as $CuNi_3Co$@NF.

3.2. Structural properties of the as-prepared $CuNi_3Co$@NF electrode

As illustrated in Fig. S6a-c, upon electrochemical co-deposition under the optimal conditions specified above, the NF branches were uniformly coated with a rough alloy layer, without visible peeling or local agglomeration. High-magnification SEM images (Fig.1b–d) reveal that the electrode surface is composed of densely stacked "cauliflower-like" particles, which grow continuously along the nickel foam branches, forming a dense and highly rough coating. Such rough hierarchical structures have been demonstrated in various foam-based metal electrodes to significantly increase the geometric and electrochemically active surface area (ECSA), which is favorable for multi-electron electrocatalytic reactions [32–34].

Statistical analysis of these microparticle sizes based on SEM images indicates that the particle size of the $CuNi_3Co$ alloys mainly centers at ~1.0 μm, with a narrow distribution of 0.8–1.2 μm (Fig. S6d), underscoring the tailorability of the nucleation and growth of the micron-sized alloys by optimizing electrodeposition conditions. The integration of macroporous NF scaffolds with micron-scale alloy particles not only shortens the diffusion paths of reactants/intermediates to active sites but also alleviates local accumulation of gaseous products, thereby improving mass transfer at the electrode interface [35,36]. EDX elemental mapping (Fig. 1e) confirms that the $CuNi_3Co$ alloy layer forms a well-conformal coating on the 3D nickel foam, with a uniform distribution of Ni, Cu, and Co over the observed region, suggesting the successful co-deposition of Cu, Ni, and Co species to form a compositionally homogeneous ternary layer rather than isolated metal domains from the NF scaffold.

XRD patterns of NF, CuNi@NF, and $CuNi_3Co$@NF exhibit characteristic diffraction peaks corresponding to the face-centered cubic (fcc) Ni phase, in good agreement with the standard PDF card (PDF #04–0850, Fig. 2a). Compared with pristine NF, the diffraction peaks of CuNi@NF and $CuNi_3Co$@NF display slight shifts in 2θ positions and noticeable changes in relative intensity, suggesting lattice distortion induced by the incorporation of Cu and Co atoms into the Ni lattice. No additional diffraction peaks attributable to crystalline Cu, Co, or their oxides (e.g., CuO, NiO, or CoO) are detected, indicating that Cu and Co do not form separate crystalline phases but are mainly incorporated into the fcc-type Ni lattice in the form of a substitutional solid solution. These observations are consistent with previous reports on Cu—Ni and Ni—Co multimetallic systems [27,37,38], and collectively suggest the formation of a Cu–Ni–Co multimetallic solid-solution structure rather than phase-segregated metals or bulk oxides.

XPS analysis was employed to investigate the surface composition and chemical states of the $CuNi_3Co$@NF electrode. The survey spectrum (Fig. 2b) reveals the presence of Cu, Ni, Co, O, and C, confirming successful co-deposition on the nickel foam surface. The surface atomic ratio of Cu:Ni:Co is approximately close to 1:3:1 (Table S2), in reasonable agreement with the nominal composition of the electrode. The high-resolution C 1 s spectrum (Fig. 2c) can be deconvoluted into C–C/C=C, C—O, and O–C=O components, mainly attributed to adventitious carbon. In the high-resolution Cu 2p spectrum (Fig. 2d), the dominant Cu $2p_{3/2}$ peak at ~932.5 eV is assigned to Cu^0/Cu^+ species; the absence of pronounced shake-up satellite peaks suggests that Cu^{2+} is not a major surface component. A weak high-binding-energy shoulder may indicate minor surface oxidation. In contrast, the Ni 2p spectrum (Fig. 2e) is dominated by Ni^{2+} species, as evidenced by the Ni $2p_{3/2}$ peak at ~855–856 eV accompanied by strong satellite features, characteristic of Ni^{2+} in an oxide/hydroxide environment. Similarly, the Co 2p spectrum (Fig. 2f) exhibits Co^{2+}-related features with pronounced satellite peaks, suggesting cobalt oxide/hydroxide species on the surface [39–41].

Taken together, XRD and XPS suggest that $CuNi_3Co$@NF consists of an fcc-type Cu–Ni–Co multimetallic solid-solution bulk, while the outer surface undergoes spontaneous oxidation/hydroxylation upon exposure to ambient conditions/electrolyte, resulting in a Cu^0/Cu^+-rich surface decorated with Ni- and Co-based oxide/hydroxide species. Such a "metallic solid-solution core–oxyhydroxide shell" configuration has been widely reported for electrodeposited multimetallic electrodes and is considered beneficial for electrochemical reactions by combining high electronic conductivity with favorable surface chemistry for proton-coupled multi-electron processes [42,43].

3.3. NO_3RR performance and activity probing of the $CuNi_3Co$@NF electrode

The NO_3RR performance of $CuNi_3Co$@NF was evaluated and compared with NF and CuNi@NF in a Cl^--free electrolyte (Fig. 3a). After 90 min of electrolysis, $CuNi_3Co$@NF achieved nearly complete NO_3^-–N removal, significantly outperforming both CuNi@NF and pristine NF under identical conditions. Meanwhile, $CuNi_3Co$@NF exhibited the highest NH_4^+–N selectivity in Cl^--free media, accompanied by minimal NO_2^-–N accumulation and negligible N_2 formation.

Compared with the binary CuNi@NF and monometallic NF electrodes, the ternary $CuNi_3Co$@NF electrode demonstrates superior NO_3RR activity and NH_4^+ selectivity, which can be attributed to the combined structural and compositional advantages of the multimetallic system [44–46]. Previous studies on multimetallic foam-based electrodes have shown that Ni-based frameworks provide a highly conductive 3D scaffold, Cu-rich sites favor NO_3^-/NO_2^- adsorption and initial reduction steps, while Co incorporation can modulate surface electronic

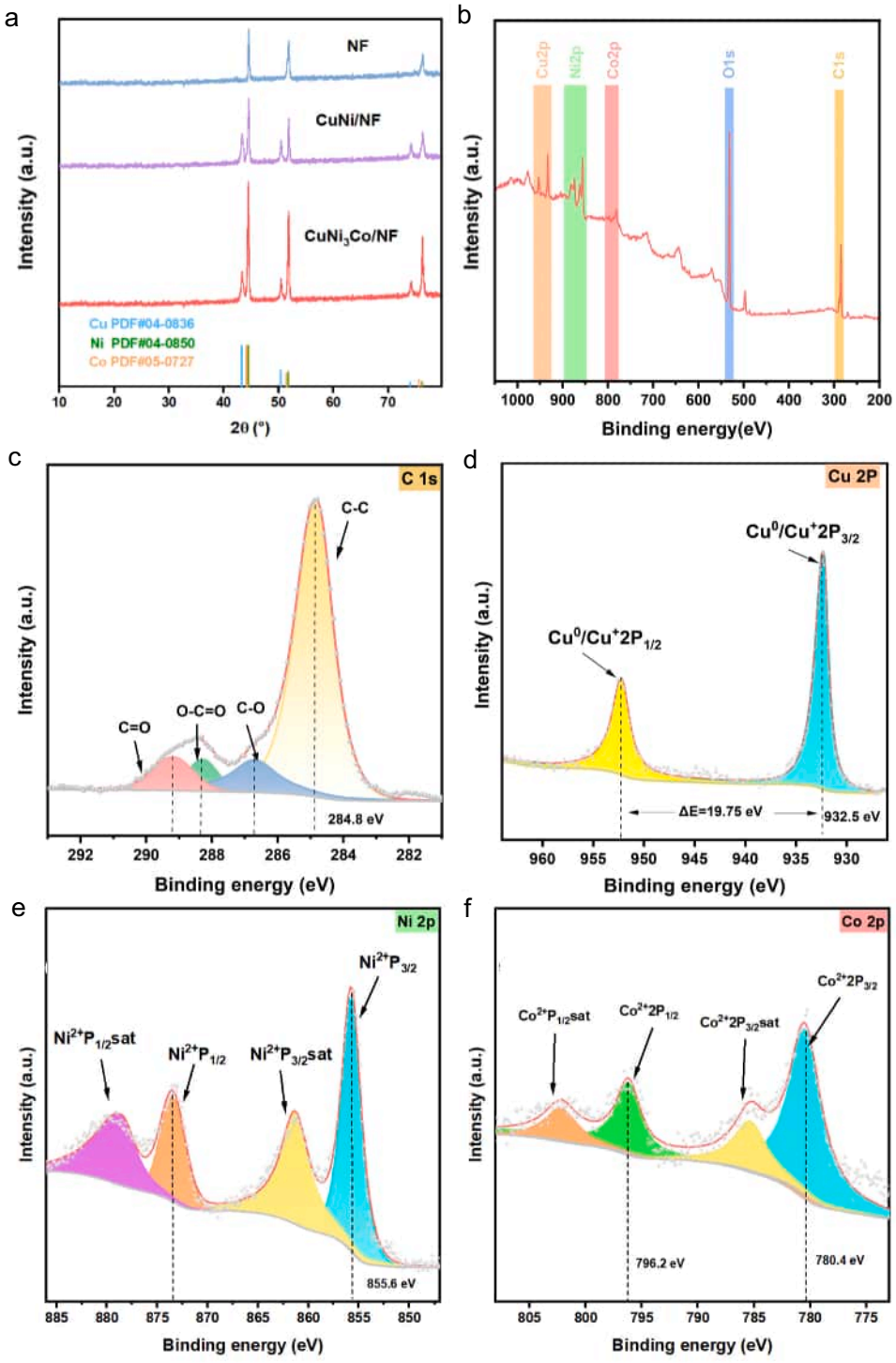

Fig. 2. (**a**) XRD patterns of NF, CuNi@NF, and $CuNi_3Co$@NF; (**b–f**) XPS spectra of the as-prepared $CuNi_3Co$@NF: (**b**) survey, (**c**) C 1 s, (**d**) Cu 2p, (**e**) Ni 2p, (**f**) Co 2p regional XPS spectra.

properties and suppress competitive hydrogen evolution reactions [22,47]. Rather than assigning distinct elementary reaction steps to individual metals, the enhanced performance of $CuNi_3Co$@NF is more reasonably understood as arising from the collective electronic interaction and geometric integration of Cu, Ni, and Co within a conformal alloy layer.

Electrochemical characterization further supports this structure–performance correlation. CV measurements with and without NO_3^- (Fig. S7d) show a pronounced cathodic current response upon NO_3^- addition, indicating strong electrochemical sensitivity of $CuNi_3Co$@NF toward nitrate species. All electrodes exhibit characteristic NO_3^- reduction features in NO_3^--containing electrolyte (Fig. 3b), confirming their intrinsic NO_3RR activity. Notably, the CV integral area follows the order of $CuNi_3Co$@NF > CuNi@NF > NF, suggesting progressively enhanced charge transfer capability and nitrate reduction activity [48].

Non-Faradaic CV analysis (Figs. S7, 3c) reveals that $CuNi_3Co$@NF

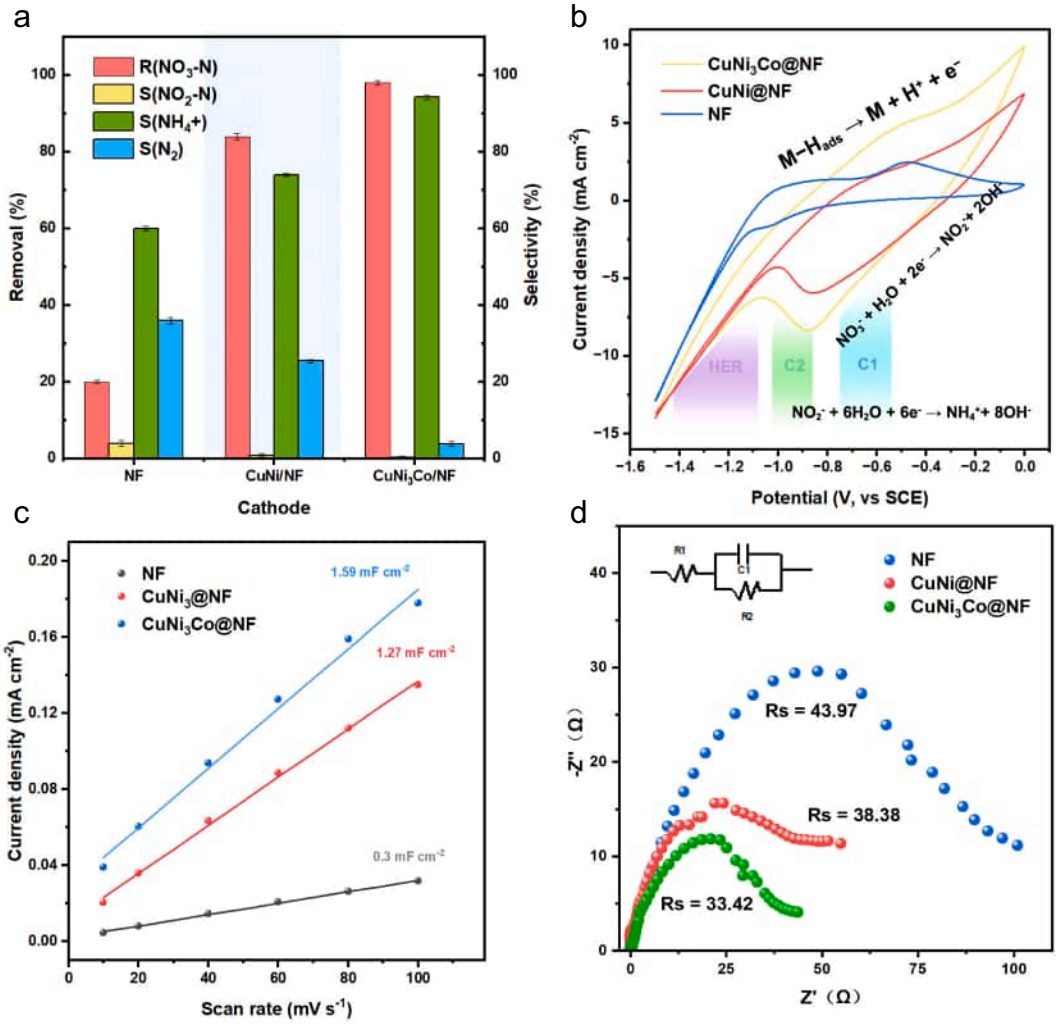

Fig. 3. (**a**) NO_3RR performance of different cathodes after the same electrolysis time (100 mL, 100 mg L^{-1} NO_3–N, 50 mM $L^{-1}Na_2SO_4$, 25 mA cm^{-2}); (**b**) CV comparison of different electrodes in 100 mL electrolyte containing 100 mg L^{-1} NO_3^-–N, 50 mM L^{-1} Na_2SO_4 and at 50 mV s^{-1}; (**c**) corresponding double-layer capacitance (C_{dl}) for $CuNi_3Co$@NF, $CuNi_3$@NF, and NF electrodes.; and (**d**) Electrochemical impedance spectra (EIS).

possesses the highest double-layer capacitance (C_{dl}), indicative of the largest electrochemically active surface area resulting from its hierarchical porous morphology [49,50]. In addition, EIS measurements in NO_3^- electrolyte (Fig. 3d) show that $CuNi_3Co$@NF exhibits the lowest charge-transfer resistance (R_{ct}), reflecting faster interfacial electron-transfer kinetics. Collectively, these electrochemical characteristics demonstrate that the superior NO_3RR performance of $CuNi_3Co$@NF primarily originates from its enlarged active surface area, improved charge-transfer efficiency, and favorable multimetallic electronic environment, rather than from a single dominant catalytic site [51].

3.4. *Effects of applied current density on NO_3RR in Cl^--free electrolyte*

To evaluate the influence of operating conditions on NO_3RR performance, the $CuNi_3Co$@NF electrode was investigated in a Cl^--free electrolyte consisting of 0.05 M Na_2SO_4 and 100 mg L^{-1} NO_3^-–N under applied current densities of 15, 25, and 35 mA cm^{-2}. Fig. 4 summarizes the temporal evolution of NO_3^-–N removal, NO_2^-–N and NH_4^+–N formation, as well as the Faradaic efficiency (FE%) toward NH_4^+–N at reaction times of 60, 90, and 120 min. As shown in Fig. 4a, increasing the current density from 15 to 25 and 35 mA cm^{-2} markedly accelerated nitrate conversion. At 15 mA cm^{-2}, NO_3^-–N removal proceeded relatively slowly, with a substantial fraction of nitrate remaining at 60 min and near-complete depletion occurring only after approximately 120 min. In contrast, nitrate concentrations decreased much more rapidly at 25 and 35 mA cm^{-2}, achieving high removal efficiencies at intermediate reaction times.

The temporal profiles of NO_2^-–N further illustrate the impact of current density (Fig. 4b). At 15 mA cm^{-2}, a pronounced NO_2^-–N accumulation peak appeared at around 40 min and decayed gradually, indicating transient accumulation of nitrite as a semi-stable intermediate. In comparison, NO_2^-–N accumulation was significantly suppressed at 25 and 35 mA cm^{-2}, with rapid disappearance of nitrite, which is consistent with faster consumption of intermediate species during nitrate reduction. Correspondingly, NH_4^+–N formation was limited at 15 mA cm^{-2} but was substantially enhanced at higher current densities, approaching nearly complete conversion to NH_4^+–N after 120 min at 25 and 35 mA cm^{-2} (Fig. 4c).

In contrast to the nitrate removal rate, the FE% toward NH_4^+–N exhibited an inverse dependence on current density (Fig. 4d). Specifically, the highest FE% values were obtained at 15 mA cm^{-2} over the entire reaction period (60–120 min), whereas higher current densities resulted in a gradual decrease in FE%. This trend can be reasonably attributed to increased contributions from competing side reactions, such as hydrogen evolution, at elevated current densities and overpotentials. In addition, FE% decreased with prolonged reaction time as

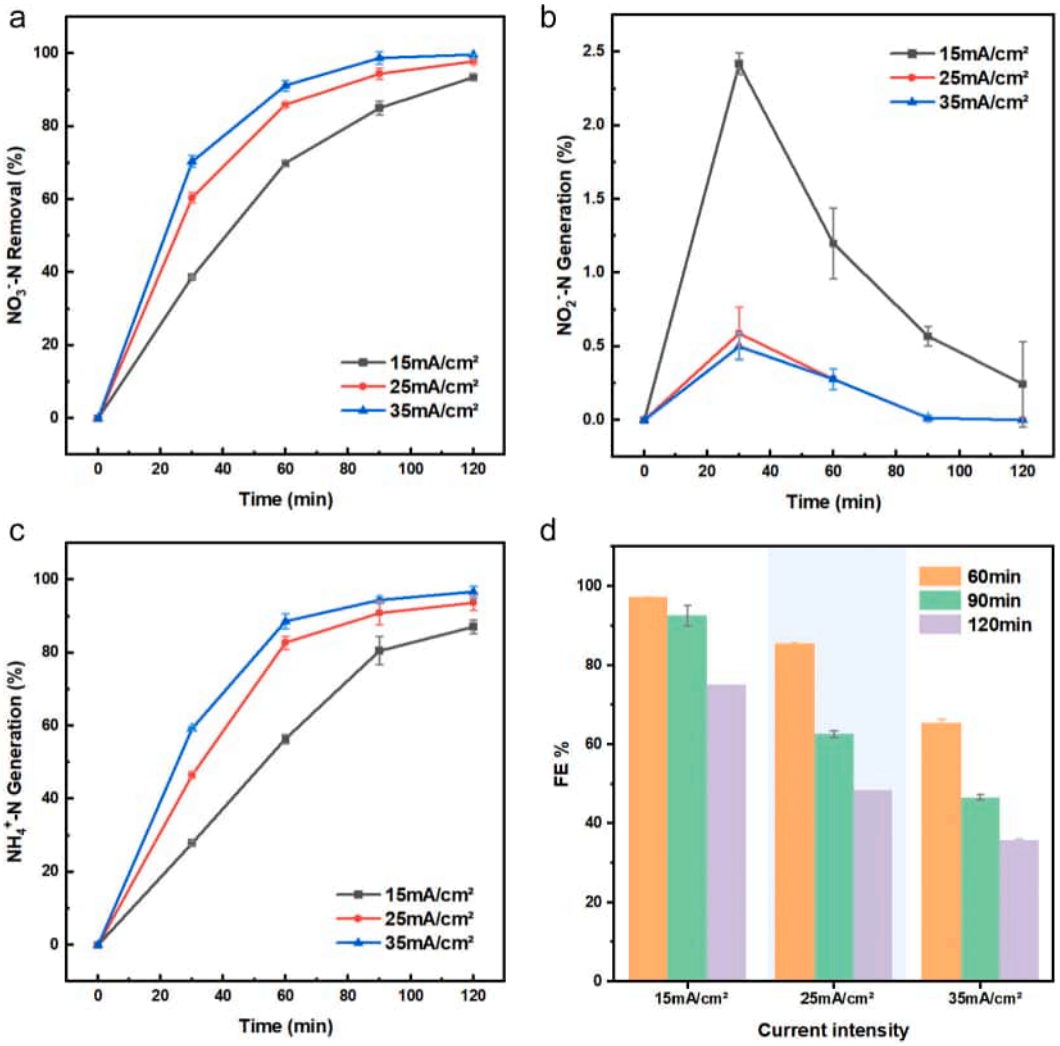

Fig. 4. Effect of applied current density on NO_3RR and nitrogen transformation using the $CuNi_3Co$@NF electrode: (**a**) NO_3^-–N removal, (**b**) NO_2^-–N formation, (**c**) NH_4^+–N generation, and (**d**) NH_4^+ Faradaic efficiency (100 mL, 100 mg L^{-1} NO_3–N, 50 mM L^{-1} Na_2SO_4).

the nitrate concentration diminished, reflecting the growing relative contribution of non-nitrate-consuming processes [52].

Overall, these results highlight an inherent trade-off between nitrate conversion rate and charge utilization efficiency. While a low current density (15 mA cm^{-2}) favors high FE%, nitrate removal and NH_4^+–N production are kinetically limited. Conversely, a high current density (35 mA cm^{-2}) enables rapid nitrate depletion but at the expense of reduced FE%. A moderate current density of 25 mA cm^{-2}, therefore, represents an optimal operational condition, balancing efficient nitrate removal with acceptable NH_4^+ yield and FE%, and was selected for subsequent NO_3RR experiments in Cl^--containing systems.

3.5. *Effects of* NO_3^-*-loading,* Cl^- *concentration, and pH on* NO_3RR *in* Cl^-*-containing wastewaters*

The effects of initial NO_3^-–N concentration (50, 100, and 300 mg L^{-1}), Cl^- concentration, and pH on nitrate reduction behavior were systematically investigated using the $CuNi_3Co$@NF electrode in Cl^--containing electrolytes. In addition, the cycling stability of the electrode was evaluated under representative operating conditions.

As shown in Fig. 5a, nearly complete NO_3^-–N removal was achieved within ≤120 min for all investigated NO_3^- loadings in 100 mL electrolyte containing 1000 mg L^{-1} NaCl at 25 mA cm^{-2}, although the reaction kinetics and nitrogen product distribution varied with the initial nitrate concentration. Specifically, a NO_3^-–N loading of 50 mg L^{-1} led to nearly complete removal within ~90 min, whereas higher loadings (100 and 300 mg L^{-1}) also reached >90% removal within 120 min, indicating the high tolerance of the $CuNi_3Co$@NF electrode toward varying nitrate concentrations.

Transient accumulation of NO_2^-–N increased with increasing NO_3^- loading, reaching a maximum at approximately 30 min (Fig. 5b), which is consistent with previous observations that higher nitrate concentrations promote nitrite formation as a reaction intermediate [53]. Similarly, NH_4^+–N exhibited a temporary increase followed by a gradual decline across all NO_3^- loadings (Fig. 5c). This behavior is consistent with a coupled reduction–oxidation process in Cl^--containing systems, in which cathodically generated NH_4^+ can be subsequently oxidized by electrochemically generated active chlorine species (Cl_2/HOCl/ClO^-) to gaseous nitrogen products, as reported in the literature [54].

As a result, the total nitrogen (TN) removal efficiency after 120 min decreased with increasing NO_3^- loading, reaching 97.7% at 50 mg L^{-1} NO_3^-–N and decreasing to 92.0% and 83.2% at 100 and 300 mg L^{-1}, respectively (Fig. 5d). This trend can be attributed to the reduced ratio of active chlorine species to nitrate at higher nitrate loadings, highlighting the importance of the Cl^-/NO_3^- ratio in determining overall TN removal efficiency in such coupled systems [54].

To further elucidate the role of Cl^- ions, the NO_3RR performance of

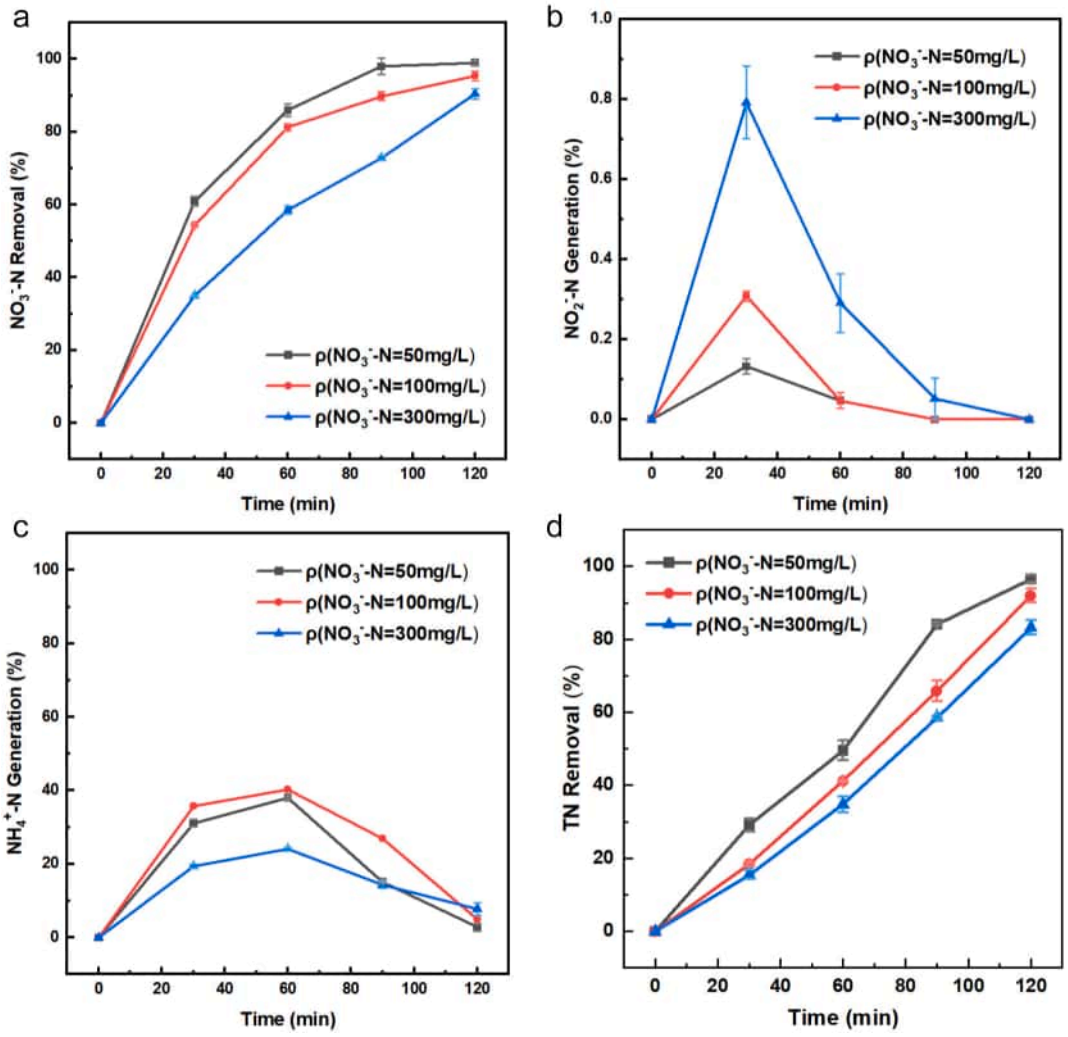

Fig. 5. Effect of initial NO_3^-–N concentration on nitrate reduction and nitrogen transformation using the $CuNi_3Co$@NF electrode: (a) NO_3^-–N removal, (b) NO_2^-–N formation, (c) NH_4^+–N formation, and (d) total nitrogen (TN) removal. Electrolysis conditions: 100 mL electrolyte, 50 mM L^{-1} Na_2SO_4, 1000 mg L^{-1} NaCl, 25 mA cm^{-2}.

$CuNi_3Co$@NF was evaluated at a fixed NO_3^-–N concentration (100 mg L^{-1}) under varying Cl^- concentrations ranging from 0 to 1500 mg L^{-1} (Fig. 6a–c), The benchmark concentrations of 100 mg L^{-1} NO_3^-–N and 0–1500 mg L^{-1} NaCl were selected to be consistent with widely adopted conditions in recent NO_3RR studies under saline/chloride-containing environments (Table S1, e.g., Refs. [17,18,20]), enabling meaningful comparison with the literature. While the NO_3^-–N removal efficiency within 120 min remained largely independent of Cl^- concentration, the distribution of nitrogen-containing products was strongly affected (Fig. 6a). In the absence of Cl^-, nitrate reduction predominantly resulted in NH_4^+ accumulation, accompanied by minimal TN removal (<10%), consistent with the Cl^--free results discussed in Section 3.3.

Upon introduction of Cl^- (500–1500 mg L^{-1}), the formation of active chlorine species enabled the rapid consumption of NO_2^- and NH_4^+ intermediates, leading to a marked increase in TN removal efficiency from ~60% at 500 mg L^{-1} Cl^- to ~90–95% at 1000–1500 mg L^{-1} Cl^- (Fig. 6a–c). These results suggest that Cl^- ions play a critical role in shifting the overall nitrogen conversion pathway from nitrate-to-ammonium accumulation toward enhanced nitrogen removal in the form of gaseous products, as widely reported for electrochemical systems coupling NO_3RR with active chlorine chemistry. Based on both NO_3RR performance and the salinity levels commonly encountered in industrial wastewaters, 1000 mg L^{-1} NaCl was selected for subsequent experiments [1,54].

The influence of pH was further investigated at 100 mg L^{-1} NO_3^-–N and 1000 mg L^{-1} NaCl (Fig. 6d–f). High NO_3^-–N removal efficiencies (>95%) were achieved across a wide pH range (3–12), with slightly enhanced performance under alkaline conditions (pH 12). Under acidic conditions (pH 3), increased accumulation of NO_2^- and NH_4^+ was observed, which is consistent with enhanced hydrogenation reactions and the greater stability of NH_4^+ at low pH, resulting in relatively lower TN removal. In contrast, neutral to alkaline conditions favor the formation and transformation of $HOCl/OCl^-$ and N—Cl intermediates, thereby facilitating more efficient nitrogen removal and suppressing residual NH_4^+ accumulation [55].

As shown in Supplementary Table S1, many recent studies have investigated nitrate reduction using electrodes in both Cl^--free and Cl^--containing systems. In this study, the $CuNi_3Co$@NF electrode demonstrated exceptionally high NH_4^+ selectivity in Cl^--free systems, highlighting its potential for ammonia resource recovery in simple nitrate wastewater. On the other hand, in complex Cl^--containing wastewater, the electrode facilitated the removal of total nitrogen (TN), achieving high nitrogen removal efficiency and meeting environmental discharge standards. This underscores the versatility of the $CuNi_3Co$@NF electrode in both scenarios, where it can either selectively generate ammonia in nitrate-rich media or achieve total nitrogen removal in Cl^--containing

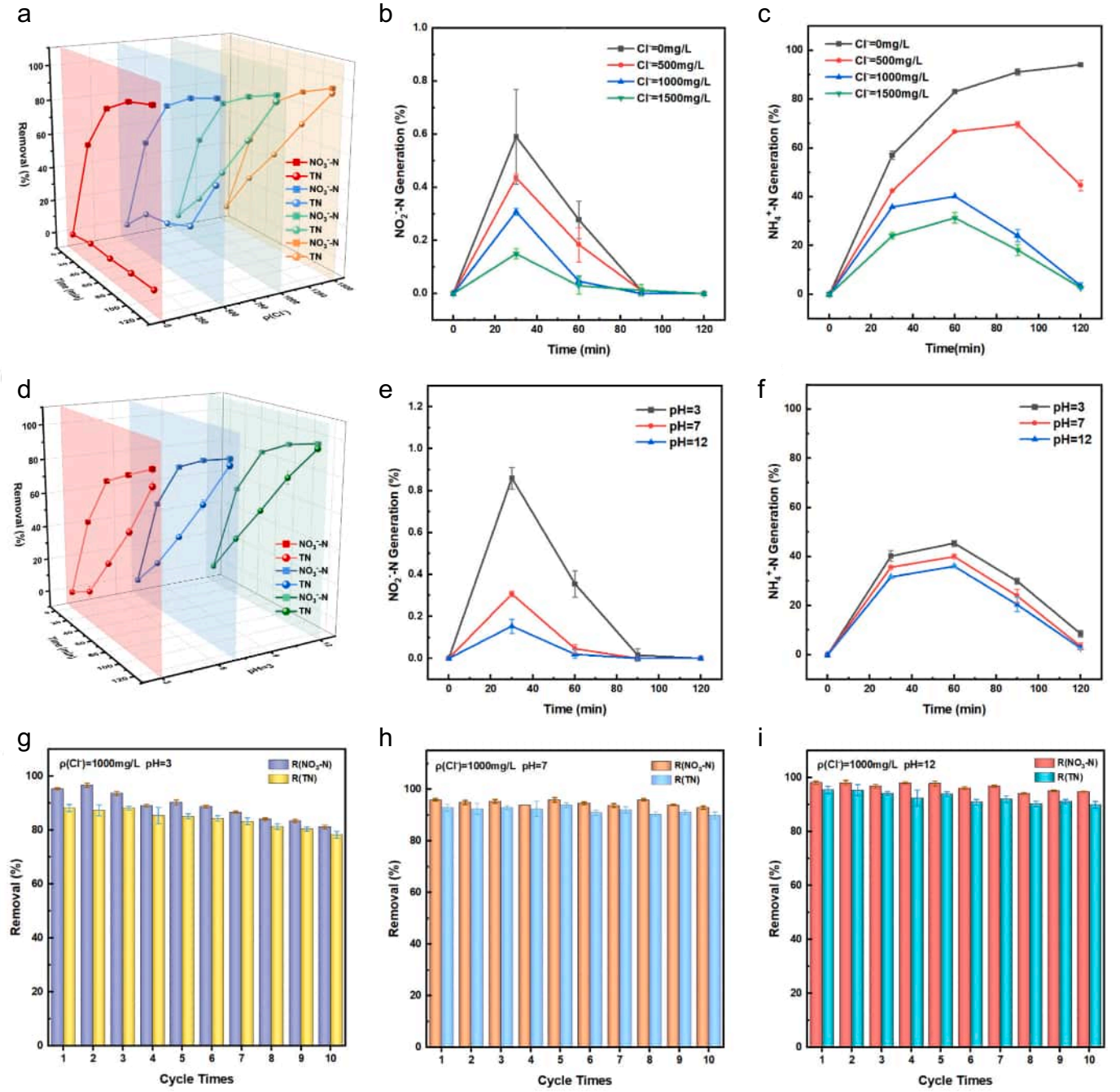

Fig. 6. Effect of Cl^- concentration on nitrate reduction and nitrogen conversion: (**a**) NO_3^-–N removal, (**b**) NO_2^-–N and NH_4^+–N formation, (**c**) total nitrogen (TN) removal; Effect of solution pH on nitrate reduction and nitrogen conversion: (**d**) NO_3^-–N removal, (**e**) NO_2^-–N and NH_4^+–N formation, (**f**) total nitrogen (TN) removal. Ten-cycle stability of $CuNi_3Co$@NF for nitrate and total nitrogen (TN) removal in chloride-containing electrolyte under different pH conditions: (**g**) pH 3, (**h**) pH 7, (**i**) pH 12. Electrolysis conditions: 100 mL electrolyte, 100 mg L^{-1} NO_3^-–N, 1000 mg L^{-1} NaCl, mA cm^{-2} using the optimized $CuNi_3Co$@NF electrode.

systems.

Finally, the cycling stability of the $CuNi_3Co$@NF electrode was evaluated over ten consecutive cycles (2 h per cycle) in Cl^--containing wastewater (100 mg L^{-1} NO_3^-–N, 1000 mg L^{-1} NaCl) at pH 3, 7, and 12 (Fig. 6g–i). Notably, a cycling number of 5–10 is commonly adopted in recent studies of nitrate electroreduction using Ni foam–based electrodes under saline or chloride-containing conditions; here, stability was intentionally assessed under more stringent pH and salinity conditions to reflect application-relevant scenarios. At pH 7, both NO_3^-–N and TN removal efficiencies remained highly stable (>90%) throughout all cycles, while similarly high performance was maintained at pH 12. A moderate decline in performance was observed under acidic conditions (pH 3), which can be reasonably attributed to enhanced surface corrosion and partial passivation in the high-Cl^- and low-pH environment [56].

Despite these harsh conditions, the $CuNi_3Co$@NF electrode consistently exhibited high NO_3RR activity and TN removal efficiency comparable to, or exceeding, many state-of-the-art electrodes reported in the literature (Table S1). This robustness is further supported by XPS analysis of the cycled electrode, which reveals only minor changes in the chemical states of Cu, Ni, and Co relative to the pristine electrode (Fig. 7a–c), ICP-OES analysis of the electrolyte (Table S3) further

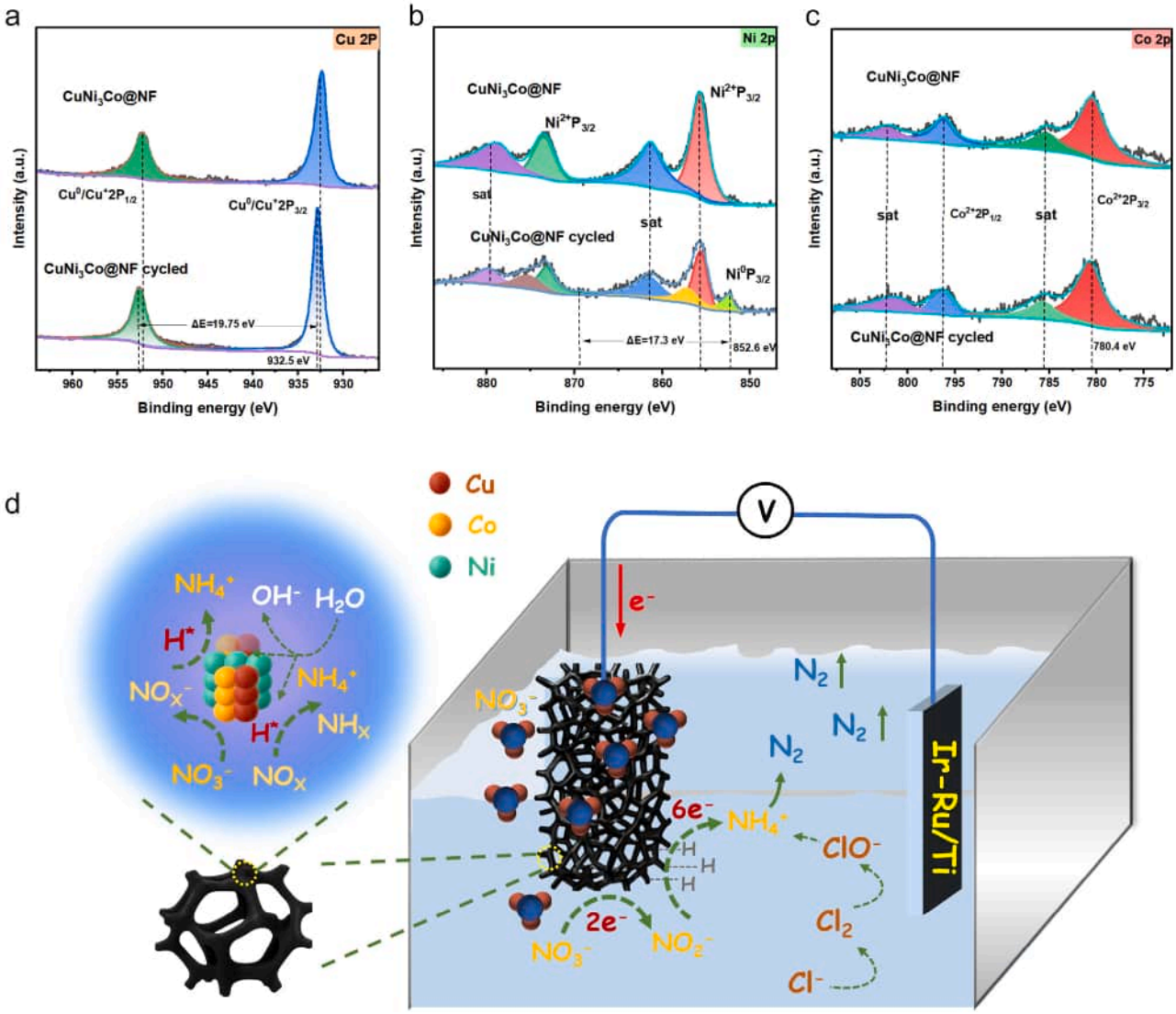

Fig. 7. (a-c) XPS high-resolution Cu 2p, Ni 2p, Co 2p spectra of the pristine and cycled $CuNi_3Co$@NF; (d) Proposed mechanism of nitrate reduction and denitrification on the $CuNi_3Co$@NF electrode.

indicates limited metal leaching during cycling: Ni and Co remain below the detection limits, while only a trace Cu concentration (0.027 mg L^{-1}) is detected after 10 cycles at pH 3, consistent with enhanced corrosion under the most acidic condition, underscoring its potential for practical remediation of Cl^--containing wastewaters [57].

3.6. *Synergistic mechanisms for NO_3RR over the $CuNi_3Co$@NF electrode*

Based on the above structural characterization, electrochemical analyses, and the product evolution in both Cl^--free and Cl^--containing systems, a plausible synergistic pathway for NO_3RR over $CuNi_3Co$@NF is proposed (Fig. 7d). The electrode comprises a conformal Cu–Ni–Co alloy layer supported on a three-dimensional nickel foam scaffold, which provides high electrical conductivity and a porous architecture favorable for electrolyte wetting and mass transport. From a qualitative perspective, and in line with prior reports on multimetallic NO_3RR catalysts, Cu-containing motifs are often associated with facilitating nitrate/nitrite adsorption and the initial reduction steps, whereas incorporating Ni/Co can tune the interfacial electronic structure and charge-transfer kinetics, which may promote subsequent multi-electron/proton-coupled transformations while mitigating competing HER [22]. Accordingly, the mechanistic roles discussed here are presented as a literature-consistent interpretation of the observed activity/selectivity trends rather than a direct identification of the real-time active state, which would require operando spectroscopy [22,58,59].

Importantly, the nanoscale uniform coexistence of Cu, Ni, and Co leads to a synergistic enhancement of interfacial kinetics, as quantitatively reflected by a larger electrochemically active surface area (higher C_{dl}), reduced charge-transfer resistance (EIS), and a more pronounced nitrate-triggered cathodic response in CV. Together, these electrochemical descriptors provide experimental evidence that the ternary Cu–Ni–Co architecture enables cooperative performance enhancement beyond binary or single-metal systems.

In Cl^--free electrolytes, nitrate reduction predominantly follows a stepwise multi-electron hydrogenation pathway ($NO_3^- \rightarrow NO_2^- \rightarrow NO \rightarrow NH_3/NH_4^+$). In this process, Cu-containing motifs are frequently correlated with facilitating nitrate/nitrite interaction and the initial reduction steps, whereas Ni/Co incorporation may contribute to subsequent hydrogenation of NO_2^- and NO intermediates, leading to NH_4^+ as the dominant dissolved product [22], accompanied by minor amounts of NO_2^- and N_2 (Eqs. 7–10).

In Cl^--containing systems, the cathodic nitrate reduction pathway remains dominated by $NO_3^- \rightarrow NH_4^+$ hydrogenation. However,

anodically generated active chlorine species (Cl_2/HOCl/OCl^-) subsequently react with cathodically produced NH_4^+ and residual NO_2^- through solution-phase reactions involving chloramine intermediates, leading to the formation of gaseous nitrogen products (Eqs. 11–13). As a result, the overall nitrogen removal process in Cl^--containing electrolytes is reasonably described as a coupled electrochemical–chemical pathway, in which the $CuNi_3Co$@NF cathode efficiently converts nitrate to reduced nitrogen species, while active chlorine species enable their further transformation at the system level [60–62]. Therefore, TN removal is used as the primary performance metric under Cl^--containing conditions. It should be noted that in a well-mixed undivided reactor, NO_3^- is continuously supplied to the cathode surface through convection and diffusion, while the cathodic consumption only establishes local concentration gradients. Moreover, the membrane-free configuration is intentionally adopted to facilitate the interaction between cathodically generated reduced-N species (NH_4^+/NO_2^-) and anodically produced reactive chlorine species, thereby enabling an EC–C coupled pathway and enhancing system-level TN removal in chloride-containing media.

Collectively, these results indicate that the $CuNi_3Co$@NF electrode functions as a highly NH_4^+-selective nitrate reduction cathode in Cl^--free environments, while enabling an efficient $NO_3^- \rightarrow NH_4^+ \rightarrow$ gaseous nitrogen removal cascade in Cl^--rich systems when coupled with anodic active chlorine chemistry. Further theoretical investigations, such as density functional theory (DFT) calculations and operando/in situ FTIR, would be valuable for elucidating the detailed energetics and elementary steps of nitrate reduction on the ternary Cu–Ni–Co surface.

$$NO_3^-(abs) + H_2O + 2e^- \rightarrow NO_2^-(abs) + 2OH^- \quad (7)$$

$$NO_2^-(abs) + H_2O + 2e^- \rightarrow NO(abs) + 2OH^- \quad (8)$$

$$NO(abs) + 5H_2O + 5e^- \rightarrow NH_4^+ + 6OH^- \quad (9)$$

$$NO_2^-(abs) + H_2O + 2e^- \rightarrow N_2(abs) + 2OH^- \ (\text{Negligible}) \quad (10)$$

$$2Cl^- \rightarrow Cl_2 + 2e^- \quad (11)$$

$$Cl_2 + H_2O \rightarrow ClO^- + 2H^+ + Cl^- \quad (12)$$

$$3ClO^- + 2NH_4^+ \rightarrow N_2 + 3H_2O + 2H^+ + 3Cl^- \quad (13)$$

4. Conclusions

In summary, a $CuNi_3Co$@NF electrode was fabricated via complexation-assisted galvanostatic electrodeposition on 3D nickel foam, forming a uniform porous ternary alloy layer with microscale homogeneity and a “metallic core + ultrathin oxide/hydroxide shell” surface configuration. Under optimized deposition conditions (0.01 M Cu^{2+}/0.20 M Ni^{2+}/0.04 M Co^{2+}, dual-anode, 25 mA cm^{-2}, 45 °C, 45 min), the electrode delivered exceptional intrinsic NO_3RR performance in Cl^--free electrolyte, achieving near-quantitative NO_3^-–N removal with ~98% NH_4^+ selectivity as the dominant aqueous product. Electrochemical analyses indicate enlarged electrochemically active surface area and accelerated interfacial charge transfer, consistent with synergistic enhancement of NO_3RR kinetics in the ternary Cu–Ni–Co architecture. In Cl^--containing nitrate wastewater, $CuNi_3Co$@NF maintained efficient NO_3^- removal across broad operating windows (50–300 mg L^{-1} NO_3^-–N, 0–1500 mg L^{-1} Cl^-, pH 3–12). Under representative saline conditions (≈1000 mg L^{-1} Cl^-) and neutral-to-alkaline pH, high TN removal was achieved with excellent multi-cycle stability. Mechanistically, the Cl^--free system is dominated by cathodic $NO_3^- \rightarrow NH_4^+$ hydrogenation, whereas in chloride-containing media the overall nitrogen removal can be described as a coupled $NO_3^- \rightarrow NH_4^+ \rightarrow$ gaseous nitrogen cascade, where anodically generated active chlorine promotes solution-phase conversion of cathodically produced NH_4^+/NO_2^-. Overall, this work presents a structurally controllable ternary alloy cathode with robust activity in saline environments and provides an application-oriented framework for high-salinity nitrate wastewater treatment.

Declaration of competing interest

The authors declare that they have no known competing financial interests or personal relationships that could have appeared to influence the work reported in this paper.

Acknowledgments

The work was partially supported by the National Natural Science Foundation of China (52000101) and the Priority Academic Program Development (PAPD) of Jiangsu Higher Education Institutions.

Appendix A. Supplementary data

Supplementary data to this article can be found online at https://doi.org/10.1016/j.seppur.2026.137342.

Data availability

Data will be made available on request.

References

[1] Q. Gao, H.S. Pillai, Y. Huang, S.K. Liu, Q.M. Mu, X. Han, Z.H. Yan, H. Zhou, Q. He, H.L. Xin, H.Y. Zhu, Breaking adsorption-energy scaling limitations of electrocatalytic nitrate reduction on intermetallic CuPd nanocubes by machine-learned insights, Nat. Commun. 13 (2022) 2338, https://doi.org/10.1038/s41467-022-29926-w.
[2] F. Rezvani, M.-H. Sarrafzadeh, S. Ebrahimi, H.-M. Oh, Nitrate removal from drinking water with a focus on biological methods: a review, Environ. Sci. Pollut. Res. 26 (2019) 1124–1141, https://doi.org/10.1007/s11356-017-9185-0.
[3] M. Cesur, A. Özgür, Application of membrane processes for nitrate (NO_3^-) removal, current Chinese, Science 3 (2023) 42–56, https://doi.org/10.2174/1573399819666220907140754.
[4] R.R. Yaragal, S. Mutnuri, Nitrates removal using ion exchange resin: batch, continuous column and pilot-scale studies, Int. J. Environ. Sci. Technol. 20 (2023) 739–754, https://doi.org/10.1007/s13762-021-03836-8.
[5] R. Zheng, K. Zhang, L. Kong, S. Liu, Research progress and prospect of low-carbon biological technology for nitrate removal in wastewater treatment, Front. Environ. Sci. Eng. China 18 (2024) 80, https://doi.org/10.1007/s11783-024-1840-3.
[6] A. Lejarazu-Larrañaga, J.M. Ortiz, S. Molina, S. Pawlowski, C.F. Galinha, V. Otero, E. García-Calvo, S. Velizarov, J.G. Crespo, Nitrate removal by Donnan dialysis and anion-exchange membrane bioreactor using upcycled end-of-life reverse osmosis membranes, Membranes 12 (2022) 101, https://doi.org/10.3390/membranes12020101.
[7] Y. Liu, J. Wang, Reduction of nitrate by zero valent iron (ZVI)-based materials: a review, Sci. Total Environ. 671 (2019) 388–403, https://doi.org/10.1016/j.scitotenv.2019.03.317.
[8] V. Rosca, M. Duca, M.T. de Groot, M.T. Koper, Nitrogen cycle electrocatalysis, Chem. Rev. 109 (2009) 2209–2244, https://doi.org/10.1021/cr8003696.
[9] W. Zhong, Z. Gong, P. Chen, Q. Cao, X. Liu, Y. Chen, Z. Lin, Electrochemical reduction of nitrate to ammonia: from fundamental understanding to practical applications, Chem. Catal. 4 (2024) 101060, https://doi.org/10.1016/j.checat.2024.101060.
[10] Z. Zhang, N. Zhang, J. Zhang, B. Deng, Z. Cao, Z. Wang, G. Wei, Q. Zhang, R. Jia, P. Xiang, S. Xia, Critical review in electrocatalytic nitrate reduction to ammonia towards a sustainable nitrogen utilization, Chem. Eng. J. 483 (2024) 148952, https://doi.org/10.1016/j.cej.2024.148952.
[11] Y. Wang, C. Wang, M. Li, Y. Yu, B. Zhang, Nitrate electroreduction: mechanism insight, in situ characterization, performance evaluation, and challenges, Chem. Soc. Rev. 50 (2021) 6720–6733, https://doi.org/10.1039/D1CS00116G.
[12] X. Lu, H. Song, J. Cai, S. Lu, Recent development of electrochemical nitrate reduction to ammonia: a mini review, Electrochem. Commun. 129 (2021) 107094, https://doi.org/10.1016/j.elecom.2021.107094.
[13] Z. Shu, H. Chen, X. Liu, H. Jia, H. Yan, Y. Cai, High-throughput screening of heterogeneous transition metal dual-atom catalysts by synergistic effect for nitrate reduction to Ammonia, Adv. Funct. Mater. 33 (2023) 2301493, https://doi.org/10.1002/adfm.202301493.
[14] Q. Wu, W. Zhu, D. Ma, C. Liang, Z. Wang, H. Liang, Screening of transition metal oxides for electrocatalytic nitrate reduction to ammonia at large currents, Nano Res. 17 (2024) 3902–3910, https://doi.org/10.1007/s12274-023-6379-2.
[15] K. Zhang, Y. Liu, Z. Pan, Q. Xia, X. Huo, O.C. Esan, X. Zhang, L. An, Cu-based catalysts for electrocatalytic nitrate reduction to ammonia: fundamentals and recent advances, EES Catal. 2 (2024) 727–752, https://doi.org/10.1039/D4EY00002A.

[16] A. Wang, J. Ye, Y. Yang, G. He, H. Chen, Recent advances in nickel-based catalysts for electrochemical nitrate reduction to ammonia, J. Ind. Eng. Chem. 132 (2024) 66–79, https://doi.org/10.1016/j.jiec.2023.11.039.
[17] Y. Shi, S. Xu, F. Li, Electrocatalytic nitrate reduction to ammonia via amorphous cobalt boride, Chem. Commun. 58 (2022) 8714–8717, https://doi.org/10.1039/d2cc02261c.
[18] Z. Bai, X. Li, L. Ding, Y. Qu, X. Chang, Artificial cu-Ni catalyst towards highly efficient nitrate-to-ammonia conversion, Sci. China-Mater. 66 (2023) 2329–2338, https://doi.org/10.1007/s40843-022-2392-8.
[19] J. Wang, J. Feng, T.-O. Soyol-Erdene, Z. Wei, W. Tang, Electrodeposited NiCoP on nickel foam as a self-supported cathode for highly selective electrochemical reduction of nitrate to ammonia, Sep. Purif. Technol. 320 (2023) 124155, https://doi.org/10.1016/j.seppur.2023.124155.
[20] Z. Chen, Y. Zhang, T. Cao, K. Yao, Electrochemical removal of nitrate using Co/Ni bimetallic electrode: high N_2 selectivity and long-term stability, Process. Saf. Environ. Prot. 179 (2023) 384–393, https://doi.org/10.1016/j.psep.2023.09.035.
[21] J.Q. Kang, Y.X. Xiao, L. Li, L.L. Qiao, C.F. Liu, C.C. Zhong, P.Z. Sun, D. Liu, W.F. Ip, H. Pan, Ternary synergy in layered double hydroxides for efficient and stable nitrate reduction, Adv. Funct. Mater. 35 (2025) 2507619, https://doi.org/10.1002/adfm.202507619.
[22] K. Zhang, G. Wei, Z. Zhang, Z. Zhao, C. Wu, Y. Liu, Y. Yang, Y. Chen, Construction of ternary alloy Cu-Ni-Co catalysts with highly active sites to enhance the initial adsorption process of nitrate reduction to ammonia, Electrochim. Acta 486 (2024) 144124, https://doi.org/10.1016/j.electacta.2024.144124.
[23] Y. Feng, T. Su, Y. Gong, H. Yu, W. Qin, M. Huo, Enhanced electrocatalytic reduction of nitrate over a ternary alloy catalyst of CuPdFe: structure, performance, and mechanism, J. Environ. Chem. Eng. 12 (2024) 112700, https://doi.org/10.1016/j.jece.2024.112700.
[24] K. Hebbache, N.A. Ahmed, N. Aliouane, M. Eyraud, K. Mira, A. Achouri, A. Djermoune, Electrodeposition of Ni-Cu alloy electrodes in sulfate-citrate medium and their use for non-enzymatic glucose oxidation, Ionics 30 (2024) 1–22, https://doi.org/10.1007/s11581-024-05526-0.
[25] S. Zhang, Z.N. Ye, M.Y. Ma, P.C. Yin, Y. Bao, F.H. Li, Optimizing the integration of nickel hexacyanoferrate with hollow mesoporous carbon spheres (HMCSs) for highly efficient capacitive deionization, Desalination 603 (2025) 118679, https://doi.org/10.1016/j.desal.2025.118679.
[26] P.C. Yin, Y.C. Yang, S. Zhang, Z. Hu, D.W. Li, F.H. Li, Oxygen vacancy-rich Ti (sub) oxide electrodes boost desalination performance on hybrid capacitive deionization (HCDI) platforms, Chem. Eng. J. 527 (2026) 171840, https://doi.org/10.1016/j.cej.2025.171840.
[27] D. Goranova, G. Avdeev, R. Rashkov, Electrodeposition and characterization of Ni–Cu alloys, Surf. Coat. Technol. 240 (2014) 204–210, https://doi.org/10.1016/j.surfcoat.2013.12.014.
[28] Z. Hu, Y. Wang, Z. Liang, H. Jin, J. Li, Z. Ning, Optimizing Ni/Ni-cu multilayer alloy coating via pulsed electrodeposition: process parameter analysis and antibacterial performance, JOM 77 (2025) 6912–6927, https://doi.org/10.1007/s11837-025-07556-z.
[29] Y. Chen, X. Wen, H. Li, F. Zhu, C. Fang, Z. Li, Z. Zhou, W. Jiang, Effects of deposition current density, time and scanning velocity on scanning jet electrodeposition of Ni-Co alloy coating, J. Manuf. Process. 101 (2023) 458–468, https://doi.org/10.1016/j.jmapro.2023.06.020.
[30] J.A.M. Oliveira, A.F. de Almeida, A.R.N. Campos, S. Prasad, J.J.N. Alves, R.A.C. de Santana, Effect of current density, temperature and bath pH on properties of Ni–W–Co alloys obtained by electrodeposition, J. Alloys Compd. 853 (2021) 157104, https://doi.org/10.1016/j.jallcom.2020.157104.
[31] L. Yang, L. Wang, C. Xing, C. Wang, S. Chang, Z. Zhao, Bubble-template assisted fast electrochemical deposition of 3-D ternary Ni-Cu-Co alloy as promising catalyst for electrochemical overall water splitting, Fuel 357 (2024) 129890, https://doi.org/10.1016/j.fuel.2023.129890.
[32] S. Mojabi, S. Sanjabi, Facile electrodeposition of feather-like Cu–Ni foam as an affordable electrocatalyst for hydrogen evolution reaction, Bull. Mater. Sci. 46 (2023) 9, https://doi.org/10.1007/s12034-022-02838-7.
[33] A. Abdelfatah, Y. Reda, R. Abdel-Karim, S.M. El-Raghy, K.M. Zohdy, Electrochemical characterization of electrodeposited Ni–Cu foams and their application as electrodes for supercapacitors, Front. Mech. Eng. 6 (2020), https://doi.org/10.3389/fmech.2020.00035, 2020.
[34] X. Zhang, Y. Li, Y. Guo, A. Hu, M. Li, T. Hang, H. Ling, 3D hierarchical nanostructured Ni–Co alloy electrodes on porous nickel for hydrogen evolution reaction, Int. J. Hydrog. Energy 44 (2019) 29946–29955, https://doi.org/10.1016/j.ijhydene.2019.09.193.
[35] L. Abbasi, M. Arvand, Engineering hierarchical ultrathin $CuCo_2O_4$ nanosheets array on Ni foam by rapid electrodeposition method toward high-performance binder-free supercapacitors, Appl. Surf. Sci. 445 (2018) 272–280, https://doi.org/10.1016/j.apsusc.2018.03.193.
[36] I.A. Poimenidis, N. Papakosta, A. Klini, M. Farsari, M. Konsolakis, P.A. Loukakos, S. D. Moustaizis, Electrodeposited Ni foam electrodes for increased hydrogen production in alkaline electrolysis, Fuel 342 (2023) 127798, https://doi.org/10.1016/j.fuel.2023.127798.
[37] Y. Chen, H. Yang, H. Feng, P. Yang, J. Zhang, B. Shu, Electrodeposition and corrosion performance of Ni-Co alloys with different cobalt contents, Mater. Today Commun. 35 (2023) 106058, https://doi.org/10.1016/j.mtcomm.2023.106058.
[38] S. Wang, X. Guo, H. Yang, J. Dai, R. Zhu, J. Gong, L. Peng, W. Ding, Electrodeposition mechanism and characterization of Ni–Cu alloy coatings from a eutectic-based ionic liquid, Appl. Surf. Sci. 288 (2014) 530–536, https://doi.org/10.1016/j.apsusc.2013.10.065.
[39] X. Wu, Z. Liu, T. Gao, Z. Li, Z. Song, J. Tang, F. Feng, C. Qu, F. Yao, C. Tang, Boosting electrocatalytic reduction of nitrate to ammonia over Co_3O_4 nanosheets with oxygen vacancies, Metals 13 (2023) 799, https://doi.org/10.3390/met13040799.
[40] W. Ding, K. Yan, Y. Li, C. Hu, H. Yi, C. Liu, C. Wang, C. Zhou, D. Ma, Electrocatalytic reduction of nitrate by Cu valence-regulated heterojunction electrode: A key role of Cu(I/II) composites and high nitrate reduction efficiency, J. Environ. Chem. Eng. 12 (2024) 114694, https://doi.org/10.1016/j.jece.2024.114694.
[41] L. Yang, F. Ru, J. Shi, T. Yang, C. Guo, Y. Chen, E. Wang, Z. Du, K.-C. Chou, X. Hou, Trifunctional electrocatalysts based on feather-like NiCoP 3D architecture for hydrogen evolution, oxygen evolution, and urea oxidation reactions, Ceram. Int. 49 (2023) 659–668, https://doi.org/10.1016/j.ceramint.2022.09.035.
[42] P. Zhang, L. Li, D. Nordlund, H. Chen, L. Fan, B. Zhang, X. Sheng, Q. Daniel, L. Sun, Dendritic core-shell nickel-iron-copper metal/metal oxide electrode for efficient electrocatalytic water oxidation, Nat. Commun. 9 (2018) 381, https://doi.org/10.1038/s41467-017-02429-9.
[43] M. Chen, S. Lu, X.-Z. Fu, J.-L. Luo, Core-Shell structured NiFeSn@NiFe (oxy) hydroxide nanospheres from an electrochemical strategy for electrocatalytic oxygen evolution reaction, Adv. Sci. 7 (2020) 1903777, https://doi.org/10.1002/advs.201903777.
[44] X. Li, Electrodeposition of multi-component alloys: Thermodynamics, kinetics and mechanism, Curr. Opin. Electrochem. 39 (2023) 101289, https://doi.org/10.1016/j.coelec.2023.101289.
[45] I. Marathe, J. Mishra, N.S. Neelam, M.K. Tripathi, Electrodeposition of multi component alloys for hydrogen evolution reaction – A review, Next Mater. 9 (2025) 101023, https://doi.org/10.1016/j.nxmate.2025.101023.
[46] D. Ahmadkhaniha, D. Ascani, M. Fedel, C. Zanella, Electrodeposition and properties of Ni-Co-W-(Mo-Cu) high/medium entropy alloy coatings deposited from an aqueous bath, Intermetallics 181 (2025) 108744, https://doi.org/10.1016/j.intermet.2025.108744.
[47] H.A. Younus, M. Al Hinai, M. Al Abri, R. Al-Hajri, Hierarchical Core-Shell Cu@Cu-Ni-Co alloy electrocatalyst for efficient hydrogen evolution in alkaline media, Energies 18 (2025) 1515, https://doi.org/10.3390/en18061515.
[48] Y.K. Chen, J.Y. Luo, L. Ling, Z.S. Zhan, J.T. Liu, Z.J. Gao, J.C.H. Lam, C.H. Feng, Y. Lei, In situ evolution of electrocatalysts for enhanced electrochemical nitrate reduction under realistic conditions, Environ. Sci. Ecotechnol. 23 (2025) 100492, https://doi.org/10.1016/j.ese.2024.100492.
[49] Y.-J. Shih, Z.-L. Wu, Y.-H. Huang, C.-P. Huang, Electrochemical nitrate reduction as affected by the crystal morphology and facet of copper nanoparticles supported on nickel foam electrodes (Cu/Ni), Chem. Eng. J. 383 (2020) 123157, https://doi.org/10.1016/j.cej.2019.123157.
[50] W. Kang, L. Yan, J. Tang, S. Wu, H. Yu, Z. Li, Electrochemical activation of graphite electrode for nitrate reduction: Energetic performance and application potential, Appl. Catal. B Environ. 329 (2023) 122553, https://doi.org/10.1016/j.apcatb.2023.122553.
[51] I. Kuznetsova, O. Lebedeva, D. Kultin, M. Mashkin, K. Kalmykov, L. Kustov, Enhancing efficiency of nitrate reduction to ammonia by Fe and Co nanoparticle-based bimetallic Electrocatalyst, Int. J. Mol. Sci. 25 (2024) 7089.
[52] Y.L. Zhang, J.Q. Xiong, B.P. Liu, S.H. Yan, Electrocatalytic nitrate reduction to ammonia by sea-urchin-like $CoNiO_2$ under mild conditions, Cell Rep. Phys. Sci. 5 (2024) 101994, https://doi.org/10.1016/j.xcrp.2024.101994.
[53] Y.M. Huang, C.H. He, C.Q. Cheng, S.H. Han, M. He, Y.T. Wang, N.N. Meng, B. Zhang, Q.P. Lu, Y.F. Yu, Pulsed electroreduction of low-concentration nitrate to ammonia, Nat. Commun. 14 (2023) 7368, https://doi.org/10.1038/s41467-023-43179-1.
[54] C.Y. Zhang, D. He, J.X. Ma, T.D. Waite, Active chlorine mediated ammonia oxidation revisited: reaction mechanism, kinetic modelling and implications, Water Res. 145 (2018) 220–230, https://doi.org/10.1016/j.watres.2018.08.025.
[55] L. Li, B.S. Lollar, H. Li, U.G. Wortmann, G. Lacrampe-Couloume, Ammonium stability and nitrogen isotope fractionations for NH_4^+–NH_3(aq)–NH_3(gas) systems at 20–70 °C and pH of 2–13: Applications to habitability and nitrogen cycling in low-temperature hydrothermal systems, Geochim. Cosmochim. Acta 84 (2012) 280–296, https://doi.org/10.1016/j.gca.2012.01.040.
[56] L. He, F. Yao, Y. Zhong, C. Tan, K. Hou, Z. Pi, S. Chen, X. Li, Q. Yang, Achieving high-performance electrocatalytic reduction of nitrate by N-rich carbon-encapsulated Ni-Cu bimetallic nanoparticles supported nickel foam electrode, J. Hazard. Mater. 436 (2022) 129253, https://doi.org/10.1016/j.jhazmat.2022.129253.
[57] M.B. Hariri, G.G. Botte, Simultaneous removal of ammonia and nitrate from wastewater using a pulse electrolysis technique, J. Electrochem. Soc. 170 (2023) 053502, https://doi.org/10.1149/1945-7111/accc57.
[58] J. Yu, Z. Xi, J. Su, L. Li, P. Jing, X. Xu, B. Liu, J. Zhang, A Cu–Co_3O_4 tandem catalyst for efficient electrocatalytic nitrate reduction at low concentration, ACS Mater. Lett. 6 (2024) 2591–2598, https://doi.org/10.1021/acsmaterialslett.4c00390.
[59] O.Q. Carvalho, R. Marks, H.K.K. Nguyen, M.E. Vitale-Sullivan, S.C. Martinez, L. Árnadóttir, K.A. Stoerzinger, Role of electronic structure on nitrate reduction to ammonium: A periodic journey, J. Am. Chem. Soc. 144 (2022) 14809–14818, https://doi.org/10.1021/jacs.2c05673.
[60] Q. Li, G.H. Liu, H. Du, G. Xian, L. Qi, H. Wang, Synergistic mechanisms between chlorine-mediated electrochemical advanced oxidation and ultraviolet light for

ammonia removal, J. Environ. Manag. 352 (2024) 120057, https://doi.org/10.1016/j.jenvman.2024.120057.
[61] H. Zhang, H. Zhou, H. Wang, Y. Wang, X. Yang, D. Wu, P. Yuan, M. He, W. Wei, T. Yang, Multihybridization for enhancing Fe-Ni bimetal electrocatalyst in water oxidation, Adv. Energy Mater. 15 (2025) 2403464, https://doi.org/10.1002/aenm.202403464.
[62] D.Z. Kong, Y.M. Zhao, R.Z. Wang, J.X. Li, J.K. Li, J. Ma, Inorganic electrified membrane: from basic science to performance translation, ACS ES&T Eng. 3 (2023) 2123–2146, https://doi.org/10.1021/acsestengg.3c00173.